7-10-2023

Atomistic simulations of twin facets associated with three-dimensional { []011 } twins in magnesium

Qiyu Zeng

Mingyu Gong

Houyu Ma

Yao Shen

Jian-feng Nie

See next page for additional authors

Authors

Qiyu Zeng, Mingyu Gong, Houyu Ma, Yao Shen, Jian-feng Nie, Jian Wang, and Yue Liu

Full Length Article

Atomistic simulations of twin facets associated with three-dimensional {$\bar{1}011$} twins in magnesium

Qiyu Zeng [a], Mingyu Gong [a,*], Houyu Ma [b], Yao Shen [a], Jian-feng Nie [c], Jian Wang [d], Yue Liu [a,*]

[a] *State Key Lab of Metal Matrix Composites, School of Materials Science and Engineering, Shanghai Jiao Tong University, Shanghai 200240, China*
[b] *Center for High-resolution Electron Microscopy (CHEM), School of Physical Science and Technology, Shanghai Tech University, Shanghai 201210, China*
[c] *Department of Materials Science and Engineering, Monash University, Victoria 3800, Australia*
[d] *Department of Mechanical & Materials Engineering, University of Nebraska-Lincoln, Lincoln, NE 68583, USA*

Abstract

Twinning is a deformation mechanism that creates three-dimensional (3D) twin domains through the migration of twin facets. This occurs via the nucleation and glide of twinning disconnections (TDs), which can pile up to create twin facets. A comprehensive understanding of twin facets associated with 3D twins, including their atomic structures and energies, is crucial for understanding deformation twinning. In this study, we propose a molecular statics/dynamics (MS/MD) approach to determine characteristic twin facets enclosing 3D non-equilibrium/equilibrium {$\bar{1}011$} twin domains, which has been much less studied than the counterpart {$\bar{1}012$} twin domains. The stability of different TD pile-up arrangement with varying line senses informs the morphology of 3D non-equilibrium twins, which are bounded by {$10\bar{1}0$}$_T$∥{$\bar{1}013$}$_M$, {$10\bar{1}1$}$_T$∥{0002}$_M$ and {$10\bar{1}3$}$_T$∥{$10\bar{1}3$}$_M$ coherent facets associated with pile-up of edge TDs, and discrete non-edge TDs aligned along CTBs with their line senses parallel to <$4\bar{5}13$>, <$1\bar{1}01$> <$5\bar{4}\bar{1}6$> <$2\bar{1}\bar{1}3$>or <$10\bar{1}2$> axes. Formation of semi-coherent facets of equilibrium twins is accompanied by rearrangement of TDs around misfit dislocations. 3D equilibrium {$\bar{1}011$} twins may comprise {$10\bar{1}1$}$_T$∥{0002}$_M$, {$14\bar{5}7$}$_T$∥{$3\bar{4}19$}$_M$, {$\bar{1}6\bar{5}7$}$_T$∥{$5\bar{6}17$}$_M$, {$\bar{1}4\bar{3}3$}$_T$∥{$3\bar{4}13$}$_M$, {$01\bar{1}0$}$_T$∥{$01\bar{1}1$}$_M$ and {$0\bar{2}21$}$_T$∥{$0\bar{2}21$}$_M$ semi-coherent facets in <$1\bar{2}10$>, <$4\bar{5}13$>, <$1\bar{1}01$>, <$5\bar{4}\bar{1}6$>, <$2\bar{1}\bar{1}3$> and <$10\bar{1}2$> axes, respectively.

© 2023 Chongqing University. Publishing services provided by Elsevier B.V. on behalf of KeAi Communications Co. Ltd.
This is an open access article under the CC BY-NC-ND license (http://creativecommons.org/licenses/by-nc-nd/4.0/)
Peer review under responsibility of Chongqing University

Keywords: Twinning; Twin boundary; Twinning disconnection; Molecular dynamics.

1. Introduction

Deformation twinning commonly takes place in hexagonal closed packed (HCP) metals, creating three-dimensional (3D) twin domains [1] and playing significant role in influencing mechanical properties of materials, such as strength, ductility and strain hardening capability [2–16] . A large body of experimental [1,17–29] and simulation [25,29–37] works studied twins in a two-dimensional (2D) manner, normally focusing on coherent twin boundaries (CTBs) and twinning disconnections (TDs) with line sense parallel to $\boldsymbol{\lambda} = \boldsymbol{\eta_1} \times \mathbf{K_1}$ (defined

by the twinning shear direction $\boldsymbol{\eta_1}$ and twin plane normal direction $\mathbf{K_1}$. TDs may distribute separately along twin plane or pile up on certain crystallographic planes to form steps and even facets. Correspondingly, twin boundaries (TBs) may deviate from the twin planes [28,30,35,38–40]. Typical twin steps/facets in hexagonal metals that can be observed in the $\boldsymbol{\lambda}$ views include {$10\bar{1}1$}$_T$∥{0002}$_M$ associated with {$\bar{1}011$} twins [22], {$10\bar{1}0$}$_T$∥{0002}$_M$ associated with {$\bar{1}012$} twins [21], and {$11\bar{2}2$}$_T$∥{0002}$_M$ associated with {$11\bar{2}2$} twins [19]. Corresponding to crystallography analysis, Hirth et al. [41] named these steps/facets coherency disclinations, that is to say, steps or facets on a twin boundary have disclination character. A disclination can be decomposed into wedge, twist and misfit components, depending on the orientation of the steps or facets. Types of disclinations with different

* Corresponding authors.
E-mail addresses: mingyugong@sjtu.edu.cn (M. Gong),
yliu23@sjtu.edu.cn (Y. Liu).

components and their corresponding stress fields further affects the symmetric/asymmetric kinetics of steps or facets [42]. The steps and facets along λ direction only possess wedge and misfit components. Therefore, their kinetics are not identical to other steps or facets. Studies on TDs with single line sense may reveal TDs' importance to the twin structure and dynamics. For instance, with electron backscatter diffraction (EBSD) characterization, Xu et al. [43] found steps/faces can promote nucleation and emission of secondary twinning during shock loading. However, the information is still insufficient to capture the inherently important 3D twin aspect.

Until now, there are few studies manifest 3D twins by EBSD analysis [44–46], molecular dynamics (MD) simulations [31,46–49] or phase field modeling [50,51]. For the EBSD analysis, morphologies of 3D twins are reconstructed by performing serial sectioning of deformed samples [44], which is extremely time-consuming. Atomistic simulations can model the atomic structures [52,53] and kinetics [50] of 3D twins. The associated difficulties lie in the construction of simulation models, i.e. obtaining accurate stress and strain field associated with 3D twins and their TBs. Gong et al. [48] obtained the atomic structure of 3D $\{\bar{1}012\}$ twins in nanoscale by applying multiple loading-unloading cycles to a twin nucleus which is created following the pure-shuffle nucleation mechanism [54]. Such approach is not general to other twinning modes since the associated nucleation mechanism is not clearly discussed. Dang et al. [47] developed a novel method to generate 3D twin domains by successively introducing TD loops followed by atomic shuffling. This method follows the shear-shuffle mechanism [34] and should be feasible to generate other 3D twins, i.e. $\{\bar{1}011\}$ [42], $\{11\bar{2}1\}$ [55] and $\{11\bar{2}2\}$ [53] twins. However, models with a 3D twin usually comprises around 10^8 atoms or more, making the computational efficiency significantly low. Recently, a phase field approach was developed to improve the computational efficiency by integrating energetic and kinetic information of different 2D twin boundaries (TBs) that enclose a 3D twin [50], successfully capturing the effects of temperature and stress on 3D twin growth., suggesting that growth of a 3D twin domain should be accomplished by the migration of TBs enclosing the domains [25,34,35,56–58]. Thus, information regarding orientation, stability, defect contents and atomic structures of TBs in 3D space is necessary to understand the evolution of 3D twin domains.

Typical TBs could be classified into (i) coherent facets with stress concentration by pileup of TDs and (ii) semi-coherent facets through stress relaxation of coherent facets. As for coherent facets, the piled-up TDs compensate for the mismatch between matrix and twinned crystals, and are accompanied by long-range stress and strain fields [30,47]. Therefore, a twin enclosed by coherent facets is in non-equilibrium state, referred to as non-equilibrium twin. As the twin grows, misfit dislocations appear on twin facets by dislocation rearrangement and/or emission of lattice dislocations [34,35,47,48] to relax the large elastic energies associated with long coherent facets, but destroy local coherency, forming semi-coherent

facets. The large disclination contents along long coherent facets can be reduced, and the net Burgers contents on the facets are nearly zero. Thus, twins enclosed by semi-coherent facets are in or near equilibrium state, referred to as equilibrium twins.

The coherent twin facets, without pinning of misfit dislocations, are normally related to rapid twin growth [47]. Mobility of a coherent facet is sensitive to its orientation [50,59] and length [47]. Orientation and length of a coherent facet are eventually affected by line sense, pile-up arrangement and number of TDs on the facet. For instance, Pearls barrier for edge TDs are higher than that for screw TDs, no matter for $\{\bar{1}011\}$ [42,60], $\{\bar{1}012\}$ [3,60,61] or $\{\bar{1}013\}$ [60] twinning, indicating faster growth along λ direction than along η_1 direction at beginning of twin development. For $\{\bar{1}012\}$ twins, coherent facets consisting TDs with the same line sense but with different pile-up arrangement exhibit dissimilar mobilities under the same stress and temperature condition [50], i.e. $\{\bar{1}010\}_T\|\{0002\}_M$ coherent facets formed by 45° arrangement of edge TDs exhibits higher mobility than $\{\bar{1}012\}_T\|\{10\bar{1}2\}_M$ coherent facets with 90° arrangement of edge TDs, while $\{1\bar{2}10\}_T\|\{\bar{1}2\bar{1}0\}_M$ coherent facets with 90° arrangement of screw TDs migrate faster than $\{\bar{1}101\}_T\|\{0\bar{1}11\}_M$ coherent facet with 49.8° arrangement of screw TDs. The effect of pile-up arrangement of TDs on facet mobility should be general to other twinning modes. Moreover, long coherent facet with more TDs normally has lower mobility than short facet with less TDs [47]. Formation of long coherent facets depends on the stability of piled-up TDs. The pileup of TDs requires a decrease in TDs' core energy, i.e. via smearing of cores onto twin facets, to overcome the repulsive force between TDs with the same Burgers vectors, and is also affected by TDs' line senses. For example, for $\{\bar{1}011\}$ twins, $\{10\bar{1}3\}_T\|\{10\bar{1}3\}_M$, $\{10\bar{1}1\}_T\|\{0002\}_M$ and $\{10\bar{1}0\}_T\|\{\bar{1}013\}_M$ coherent facets containing edge TDs are stable while the coherent facets containing screw TDs easily degenerate [42]. For $\{\bar{1}012\}$ twins, $\{\bar{1}010\}_T\|\{0002\}_M$ coherent facets formed by pileup of edge TDs are stable while $\{\bar{1}101\}_T\|\{0\bar{1}11\}_M$ and $\{1\bar{2}10\}_T\|\{\bar{1}2\bar{1}0\}_M$ coherent facets formed by pileup of screw TDs dissociate into multiple separated small steps after relaxation [59]. Therefore, one need to evaluate the stability associated with different pile-up arrangement of TDs with different line sense (edge, mixed or screw) before studying evolution of 3D non-equilibrium twins.

When semi-coherent twin facets build with formation of misfit dislocations on long coherent twin facets, the pile-up arrangement of TDs is likely to vary due to attraction between misfit dislocations and TDs. For example, Leu-et al. [62] proposed that stress relaxation facilitated by free surface can help rearrangement of short facets into long facets, which is proved by atomistic simulations [47]. So, one cannot simply predict pile-up arrangement of TDs on semi-coherent twin facets based on the knowledge of coherent twin facets.

The aforementioned points suggest that formation of coherent or semi-coherent twin facets in 3D space is an outcome of pile-up arrangement of TDs with different line sense, which might be revealed by high resolution transmission elec-

tron microscopy (HRTEM). Majority of the HRTEM studies characterize twin facets along the $\boldsymbol{\lambda}$ directions [1,17–27]. Recently, HRTEM studies successfully characterized atomic structures of twin facets lying non-parallel to $\boldsymbol{\lambda}$ directions for $\{\bar{1}012\}$ [52,63] and $\{11\bar{2}2\}$ [53] twins. Within our knowledge, Liu et al. [63], for the first time, experimentally explored the atomic structure of lateral side of $\{\bar{1}012\}$ twins by choosing the $\boldsymbol{\eta_1}$ direction as zone axis, and characterized two twin facets as $\{1\bar{2}10\}_T\|\{1\bar{2}10\}_M$ and $\{0\bar{1}11\}_T\|\{\bar{1}101\}_M$ interfaces. Later on, Wang et al. [52] systematically examined twin facets of $\{\bar{1}012\}$ twins in a quasi-three-dimensional manner by adopting multiple observation directions in 3D space, and characterized five more twin facets in the view normal to $<2\bar{2}01>$, $<5\bar{4}13>$ and $<4\bar{2}\bar{2}3>$ directions. Similar approach was employed to characterize twin facets of 3D $\{11\bar{2}2\}$, which is bounded by six low-index interfaces [53]. Those characterizations provide basis for further studies on kinetics of twin facets via atomistic simulations [50]. However, it should be noted that the observation directions are not arbitrary. Atomic-scale resolution of HRTEM cannot be obtained when zone axes with relatively higher indices are employed [64], thus it is impossible to reveal any twin facets lying parallel to those axes. What's more, coherent twin facets are less likely to be characterized since the stored stress can easily be relaxed by free surfaces of HRTEM thin foils [65].

In addition to HRTEM, atomistic simulations are feasible to capture the pile-up features of TDs by taking into account the energetics, i.e. interaction energy between TDs, interface energy of twin facets, ledge energy between twin facets and CTBs, and etc. It should be noted that twin facets lying parallel to high-index zone axes via pile-up of TDs with high-index line sense can be simulated by adopting periodic boundary conditions along the high-index zone axes. Moreover, the non-equilibrium state associated with coherent twin facets, which can hardly be restored in HRTEM samples, can be captured in time-scale of atomistic simulations.

In this work, we proposed a molecular statics/dynamics (MS/MD) approach to predict twin coherent/semi-coherent facets enclosing a 3D non-equilibrium/equilibrium twin domain in HCP metals by evaluating different pile-up arrangement of edge/screw/mixed TDs with/without presence of misfit dislocations. The $\{\bar{1}011\}$ twins with few understandings of its 3D character is chosen as an example to illustrate the approach. Six zone axes, $<1\bar{2}10>$, $<4\bar{5}13>$, $<1\bar{1}01>$, $<5\bar{4}\bar{1}6>$, $<2\bar{1}\bar{1}3>$ and $<10\bar{1}2>$ directions, are selected. Twin facets enclosing a non-equilibrium twin are different from those enclosing an equilibrium twin in orientation, defect contents and atomic structures. Microscopy characterization of $\{\bar{1}011\}$ twin facets in Mg alloys was performed to calibrate the prediction.

2. Methodologies

2.1. Pile-up arrangement of TDs

Apart from CTBs exactly normal to $\mathbf{K_1}$ directions, all TBs are composed of TDs. TDs associated with $\{\bar{1}011\}$ twins suc-

Table 1

Ratio between edge and screw components with respect to TD's line sense.

Line sense	$|TD_{edge}|$ (nm)	$|TD_{screw}|$ (nm)	$|TD_{edge}|/|TD_{screw}|$
$<1\bar{2}10>$	1.33	0.00	/
$<4\bar{5}13>$	1.07	0.79	1.36
$<1\bar{1}01>$	0.84	1.03	0.82
$<5\bar{4}\bar{1}6>$	0.64	1.17	0.54
$<2\bar{1}\bar{1}3>$	0.35	1.28	0.27
$<10\bar{1}2>$	0.00	1.33	0.00

cessively glide on twinning planes (the green plane normal to $\mathbf{K_1}$ direction in Fig. 1(a)). Its Burgers vector is along $\boldsymbol{\eta_1}$ direction. Character of TDs depends on their line senses, which are likely to locate along directions with relatively low crystallographic index. Fig. 1(b) shows the atomic configuration in the $\{\bar{1}011\}$ twinning plane. Six crystallographic directions are defined (Table 1). When line sense is along $<1\bar{2}10>$ direction, a TD is of edge type. A screw TD has line sense parallel to $<10\bar{1}2>$ direction. Besides, line senses could be $<4\bar{5}13>$, $<1\bar{1}01>$, $<5\bar{4}\bar{1}6>$ or $<2\bar{1}\bar{1}3>$ directions, which are 36.4°, 50.8°, 61.5° and 74.8° deviated from the $<1\bar{2}10>$ direction, respectively. Correspondingly, TDs are of mixed type. The edge, mixed and screw character affects TDs' core structure [66], thus altering TDs' motion and pile-up arrangement of TDs.

The pile-up arrangement and motion of TDs during development of a twin can be described by Fig. 1(c) or (d), depending on whether the TDs can pile up. For a rapid-growing non-equilibrium twin, TDs tend to repel each other since they share the same signed Burger vectors. According to theory of dislocations [67], only the vertical dislocation wall is stable if energies other than interaction energy between dislocations are not considered. Coherent facets by pile-up of TDs (Fig. 1(c_1)) are stable if the interface energy associated with the facets is low enough to create meta-stable state to overcome TDs' repelling force. A non-equilibrium twin coverts to its equilibrium form by stress relaxation. Correspondingly, the coherent facets transform to the semi-coherent facets accompanied by formation of misfit dislocations (Fig. 1(c_2)). The index of the semi-coherent facets is likely to be the same as the coherent facets since long facets usually have high kinetic barriers [47]. The semi-coherent facets have to depin from the misfit dislocations for further migration, and will transform back to their coherent forms (Fig. 1(c_3)).

In contrast, when an array of TDs cannot pile up, multiple short steps or facets bonding high-index crystallographic planes should be observed (Fig. 1(d_1)). It is noted that semi-coherent facets should form after stress relaxation of non-equilibrium twins because the misfit dislocations attract high-mobility discrete TDs (Fig. 1(d_2)) [47]. In this case, the change of energy within system should be mainly taken account of. Generally, facets bonding planes with lower index have smaller interface energy, are likely to form. It can be easily imagined that the semi-coherent facets will decompose to discrete TDs after depinning from the misfit dislocations (Fig. 1(d_3)).
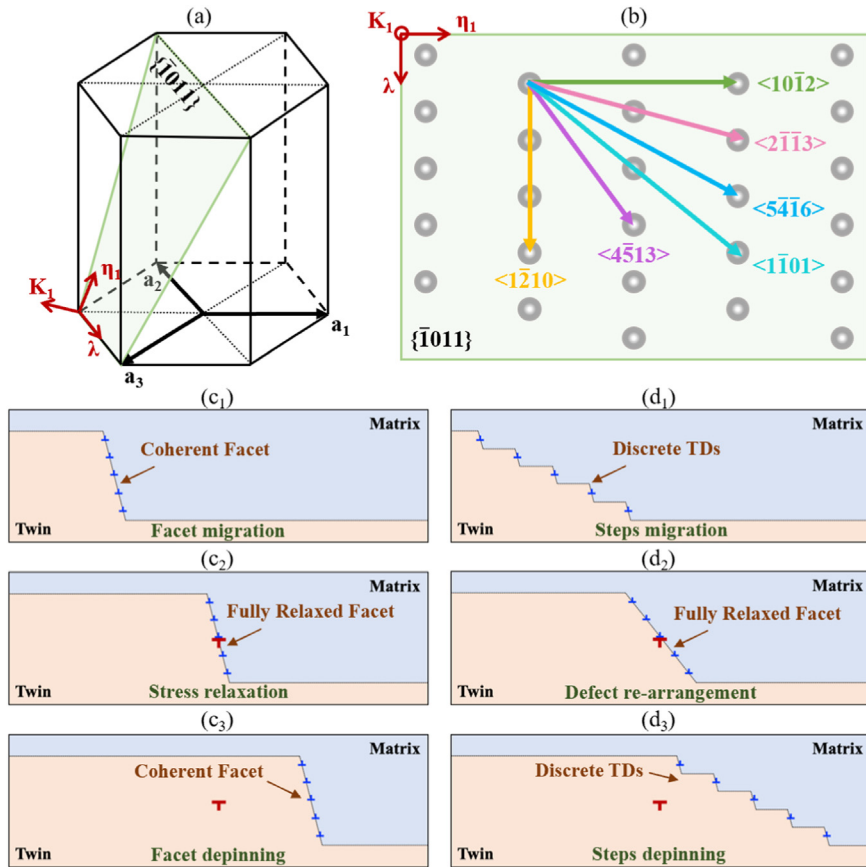
Fig. 1. (a) The HCP unit cell showing twin elements associated with $\{\bar{1}011\}$ twins. (b) Atomic configuration in the $\{\bar{1}011\}$ twinning plane and low-index crystallographic directions. Schematics depicting (c$_1$) a coherent facet transforms to (c$_2$) a semi-coherent facet via stress relaxation, and then back to (c$_3$) a coherent facet after depinning from the misfit dislocation. Schematics depicting (d$_1$) an array of discrete TDs transforms to (d$_2$) a semi-coherent facet via stress relaxation and defect re-arrangement, and then back to (d$_3$) an array of discrete TDs after depinning from the misfit dislocation.

Based on the above description, we propose a strategy to predict twin facets that enclose a 3D twin. For non-equilibrium twins, whether a coherent facet may exist depends on the arrangement (pile-up or discrete) of TDs. So, the stability of the TD pile-up along possible facets bonding low-index crystallographic planes in twin and matrix should be examined. For an equilibrium twin, formation of semi-coherent facets can be treated as evolution of coherent facets or discrete TDs after stress relaxation. Therefore, the dynamic evolution of coherent facets or discrete TDs after formation of misfit dislocations should be checked.

2.2. Atomistic simulations

MS/MD simulations were conducted for Mg with the empirical interatomic potential developed by Liu et al. [34]. The construction of models containing steps/facets of non-equilibrium twins starts with a bicrystal with $(\bar{1}011)$ twin orientation. The models adopt the coordinate that y-axis is along $\mathbf{K_1}$ direction, z-axis is along one of the low-index crystallographic directions on $(\bar{1}011)$ plane as shown in Fig. 1(b), and x-axis is cross-product of y- and z-axis. Dimensions of the models are 40 nm in x- and y-direction, and vary in z-

direction with different z-axis adopted. To create a coherent facet with total height equal to 16 $(\bar{1}011)$ interplanar distances, four TDs with $0.113[\bar{1}01\bar{2}]$ Burgers vector and 4-layer step are introduced on every four $(\bar{1}011)$ plane by applying the anisotropic Barnett-Lothe solution [68] followed by atomic shuffles [3]. By changing the alignment of TDs, the angle θ between the normal direction of twin facet and twin plane is changed. To relax the constructed coherent facets, dynamic quenching is performed until the maximum force is less than 5 pN with fixed boundaries in x- and y-directions and periodic boundary condition in z-direction.

The construction of models containing semi-coherent facets associated with equilibrium twins starts with the stable or meta-stable coherent facets. One misfit dislocation with $0.221[01\bar{1}2]$ Burgers vector is introduced for every two TDs, decreasing total Burgers content of the facet to nearly zero. As reported by previous works [69], formation of misfit dislocations is realized by dislocation rearrangement and/or emission of lattice dislocations. So, in our models, Burgers vector of the misfit dislocation is equal to the sum of two $\langle a \rangle$ dislocations in twin and matrix. The semi-coherent facets are then relaxed at 300 K for 500 ps, and then dynamically quenched. The same boundary condition as the cases of coherent facets is adopted.

2.3. Materials preparation and characterization

The Mg-0.2 at.% Gd ingot specimens were used for present investigation. The specimens were firstly extruded at 300 °C. The as-extruded specimens were compressed by 8% at room temperature along extrusion direction. For high-annular dark-field scanning transmission election microscope (HAADF-STEM) characterization, sequential aging (275 °C for 1 h) was carried out for twin boundary Gd atom segregation. Samples used for HAADF-STEM imaging were cut into 0.5 mm thick slices using Struers Accutom 50. Discs of 3 mm diameter were punched from these slices, then twin-jet electropolished using Struers Tenupol-5 in a solution of 5.3 g lithium chloride, 11.2 g magnesium perchlorate, 500 ml methanol, and 100 ml 2-butoxy-ethanol, at −55 °C and 0.1 A. HAADF-STEM was undertaken on a double Cs-corrected FEI 80–300 Titan[3] operated at 300 kV. A 15 mrad convergence semi-angle was used, corresponding to 0.12 nm resolution, with an inner-collection semi-angle of 62 mrad. For clarity, the atomic-scale HAADF-STEM images were Fourier-filtered by masking the corresponding diffraction pattern from the original image and back-transforming using a Gatan Digital Micrograph. In addition, a commercial program, a Digital Micrograph plug-in (DM 1.8.3 package, HREM Research Inc.), was used for geometric phase analysis (GPA) of an atomic-scale HAADF-STEM image. A scale range of −10% to +10% was applied to the strain map. Perforation of 3 mm disk specimen (former polished to a thickness of ∼40 μm) by ion milling was carried out with low-angle (3°) and low energy (3 keV) ion-beam. High-resolution transmission electron microscope (HRTEM) and HAADF-STEM were carried out on a JEOL-2100F electron microscope with a voltage of 200 kV. $\{\bar{1}011\}$ twins and the associated facets are characterized along <$1\bar{2}10$>, <$0\bar{1}11$> and <$10\bar{1}2$> directions, in which atomic-scale resolution can be achieved. The lattice constant ($a = b = 3.21$ Å, $c = 5.21$ Å, $\alpha = \beta = 90°$, $\gamma = 120°$) is selected for pole figure and diffraction pattern analysis of $\{\bar{1}011\}$ twin in Mg.

3. Twin facets enclosing non-equilibrium twins

3.1. Coherent facets lying parallel to <$1\bar{2}10$> axis

Twin facets lying parallel to <$1\bar{2}10$> axis contain edge TDs with line sense along <$1\bar{2}10$> axis. Whether the edge TDs can pile up depends on the arrangement of TDs, which changes with angle θ. Fig. 2(a)-(e) manifests typical arrangement of the edge TDs. Formation of $\{10\bar{1}3\}_T\|\{10\bar{1}3\}_M$ (Fig. 2(a)), $\{30\bar{3}5\}_T\|\{10\bar{1}2\}_M$ (Fig. 2(b)), $\{10\bar{1}1\}_T\|\{0002\}_M$ (Fig. 2(c)) and $\{10\bar{1}0\}_T\|\{\bar{1}013\}_M$ (Fig. 2(d)) coherent facets takes place when TDs' initial arrangement θ is set as 0.0°, 16.8°, 31.1° and 63.9°. It is noted that pile-up of edge TDs results in tilt of nearby planes in both twin and matrix, compensating for the mismatch between planes in twin and matrix bonded by the facets and maintaining the coherency. Interestingly, obvious core structure associated with TDs are no longer visible because the cores smear onto twin facets. With increasing value of θ, coherent facets no longer form. Instead,
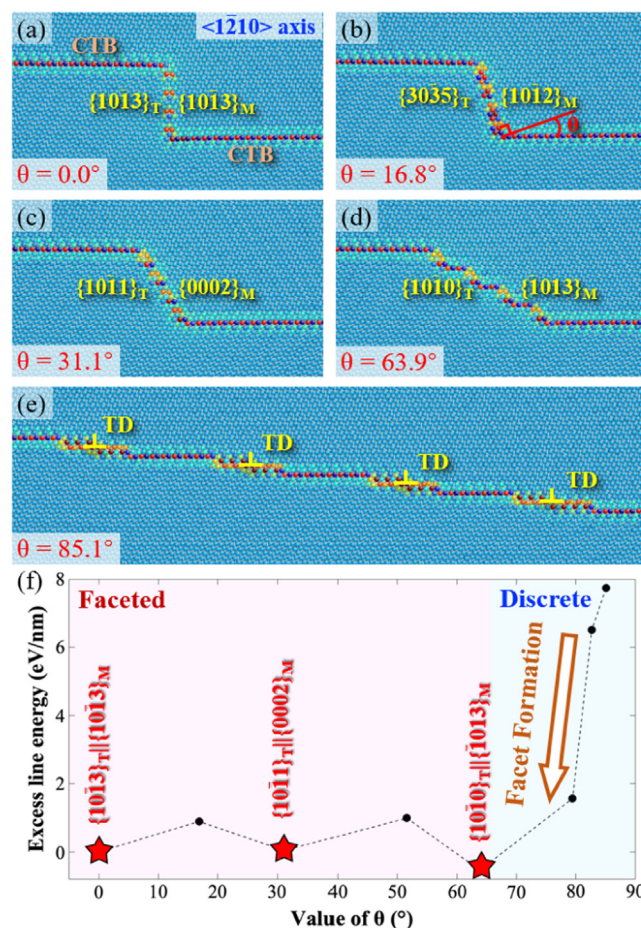

Fig. 2. Relaxed structures of (a) $\theta = 0.0°$, (b) $\theta = 16.8°$, (c) $\theta = 31.1°$, $\theta = 63.9°$ and (e) $\theta = 85.1°$ arrangement of edge type TDs with line sense parallel to <$1\bar{2}10$> axis. (f) Excess line energy of structures with respect to value of θ. The structure in (a) is set as the reference. The star label denotes coherent facets with local energy minima.

as shown in Fig. 2(e), discrete TDs align along CTBs. Obvious core structure associated with each edge TD can be observed.

Energies of structures with different edge TDs' alignment are compared. Total potential energy of the structure with $\theta = 0.0°$ is taken as reference. Since number of atoms and free surface configurations normal to x- and y-directions are the same for all structures, the energy difference is contributed by differences in interface energy, ledge energy and elastic energy associated with different TDs' arrangement. Fig. 2(f) shows excess line energy of structures with respect to value of θ. When θ is lower than 65°, coherent facets form. In this range, local energy minima are found for $\theta = 0.0°$ ($\{10\bar{1}3\}_T\|\{10\bar{1}3\}_M$), 31.1° ($\{10\bar{1}1\}_T\|\{0002\}_M$) and 63.9° ($\{10\bar{1}0\}_T\|\{\bar{1}013\}_M$). Crystallographic index of corresponding coherent facets is lower than that of the other coherent facets, i.e. $\{30\bar{3}5\}_T\|\{10\bar{1}2\}_M$ for $\theta = 16.8°$ and $\{50\bar{5}2\}_T\|\{\bar{1}015\}_M$ for $\theta = 53.0°$. When θ is larger than 65°, discrete edge TDs along CTBs are observed. Within this range, the excess line energy increases with increasing value of θ, indicating that an array of discrete edge TDs is energet-
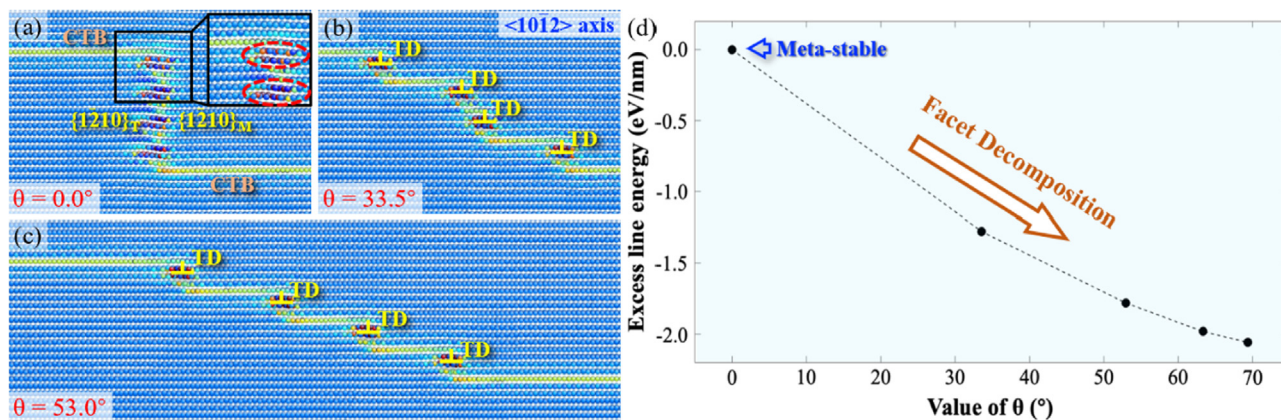
Fig. 3. Relaxed structures of (a) $\theta = 0.0°$, (b) $\theta = 33.5°$ and (c) $\theta = 53.0°$ arrangement of edge type TDs with line sense parallel to $<10\bar{1}2>$ axis. (d) Excess line energy of structures with respect to value of θ. The structure in (a) is set as the reference.

ically unfavorable. For example, after relaxation at 300 K for 200 ps, an array of discrete edge TDs as shown in Fig. 2(e) transforms to the $\{10\bar{1}0\}_T\|\{\bar{1}013\}_M$ coherent facet as shown in Fig. 2(d) via rearrangement of TDs. The results suggest that edge TDs are more likely to pile up than to dissociate for non-equilibrium $\{\bar{1}011\}$ twins.

3.2. Coherent facets lying parallel to $<10\bar{1}2>$ axis

When TDs' line sense is along $<10\bar{1}2>$ axis, they are of screw type. Twin facets containing screw TDs are parallel to $<10\bar{1}2>$ axis. According to crystallographic analysis, possible coherent facets with low-index are $\{1\bar{2}10\}_T\|\{1\bar{2}10\}_M$, $\{0\bar{2}21\}_T\|\{0\bar{2}21\}_M$ and $\{\bar{4}223\}_T\|\{\bar{4}223\}_M$ coherent interfaces corresponding to $\theta = 0.0°$, 33.5° and 53.0°. Fig. 3(a)-(c) shows the atomic structures of configurations with screw TDs' arrangement $\theta = 0.0°$, 33.5° and 53.0°. It is found that the $\{1\bar{2}10\}_T\|\{1\bar{2}10\}_M$ coherent facet as shown in Fig. 3(a) with vertical TD arrangement is stable after relaxation at 0 K. Different from the edge TDs with smeared cores onto coherent facets lying parallel to $<1\bar{2}10>$ axis (Fig. 2(a)-(d)), the screw TDs along the vertical $\{1\bar{2}10\}_T\|\{1\bar{2}10\}_M$ coherent facet exhibit observable cores as marked by the red dashed oval in the inserted figure in Fig. 3(a). The atomic structure indicates that the $\{1\bar{2}10\}_T\|\{1\bar{2}10\}_M$ coherent facet is in meta-stable state, and will easily dissociate into discrete TDs with any disturbance, i.e. thermal fluctuation or external loading. In Fig. 3(b) and (c), structures with initial TDs' arrangement $\theta = 33.5°$ and 53.0° are not stable. Screw TDs tend to repel each other, thus increasing the value of θ.

Fig. 3(d) compares the excess line energies associated with structures with different initial screw TDs' arrangement. The structure as shown in Fig. 3(a) is set as the reference. The excess line energy continuously decreases with increasing value of θ, showing opposite trend to the curve associated with edge TDs (Fig. 2(f)). So, the vertical arrangement of TDs as shown in Fig. 3(a) is in high-energy state, and will degenerate into discrete TDs, which repel each other. This process can be reproduced by heating the structure to 300 K. The results

suggest that the migrating screw TDs are more likely to be separated.

3.3. Coherent facets lying parallel to $<4\bar{5}13>$, $<1\bar{1}01>$, $<5\bar{4}\bar{1}6>$ or $<2\bar{1}\bar{1}3>$ axis

TDs are of mixed type if their line senses are neither along $<1\bar{2}10>$ axis nor along $<10\bar{1}2>$ axis. The mixed TDs are rarely discussed in previous studies. Line senses of mixed TDs are more likely to align with low-index crystallographic directions, which are $<4\bar{5}13>$, $<1\bar{1}01>$, $<5\bar{4}\bar{1}6>$ or $<2\bar{1}\bar{1}3>$ direction on $\{\bar{1}011\}$ planes. The ratio between edge and screw components varies with change of line sense, and are shown in Table 1.

Twin facets containing mixed TDs are parallel to the line sense of these TDs. Their energies vary with arrangement of TDs. Energies of twin facets lying parallel to the same zone axis are compared with the $\theta = 0.0°$ configuration set as reference. As shown in Fig. 4(a), excess line energies decrease with increasing value of θ for all studied mixed TDs, manifesting similar trend to the curve associated with screw TDs (Fig. 3(d)). Consequently, the low-index coherent facets, such as $\{11\bar{2}1\}_T\|\{0\bar{1}13\}_M$ facet (Fig. 4(b$_1$)) parallel to $<4\bar{5}13>$ axis, $\{11\bar{2}0\}_T\|\{\bar{1}\bar{1}23\}_M$ facet (Fig. 4(c$_1$)) parallel to $<1\bar{1}01>$ axis, $\{12\bar{3}0\}_T\|\{0\bar{2}23\}_M$ facet (Fig. 4(c$_1$)) parallel to $<5\bar{4}\bar{1}6>$ axis and $\{01\bar{1}0\}_T\|\{01\bar{1}\bar{1}\}_M$ facet (Fig. 4(c$_1$)) parallel to $<2\bar{1}\bar{1}3>$ axis, are unstable at 300 K and dissociate into discrete TDs as shown in Fig. 4(b$_2$)-(d$_2$) no matter the associated edge-to-screw ratio. What's more, the curves associated with different zone axis in Fig. 4(a) are the same to some extent (confined in the blue region). This is because the elastic interaction energies, which is mainly affected by Burgers vectors and distances, between TDs are dominant.

3.4. Remarks on twin facets enclosing non-equilibrium twins

Based on the analysis presented above, possible twin facets that enclose 3D non-equilibrium $\{\bar{1}011\}$ twins are schematically summarized in Fig. 5(a). Edge TDs may pile up, forming $\{10\bar{1}0\}_T\|\{\bar{1}013\}_M$ (Fig. 5(b$_1$)), $\{10\bar{1}1\}_T\|\{0002\}_M$
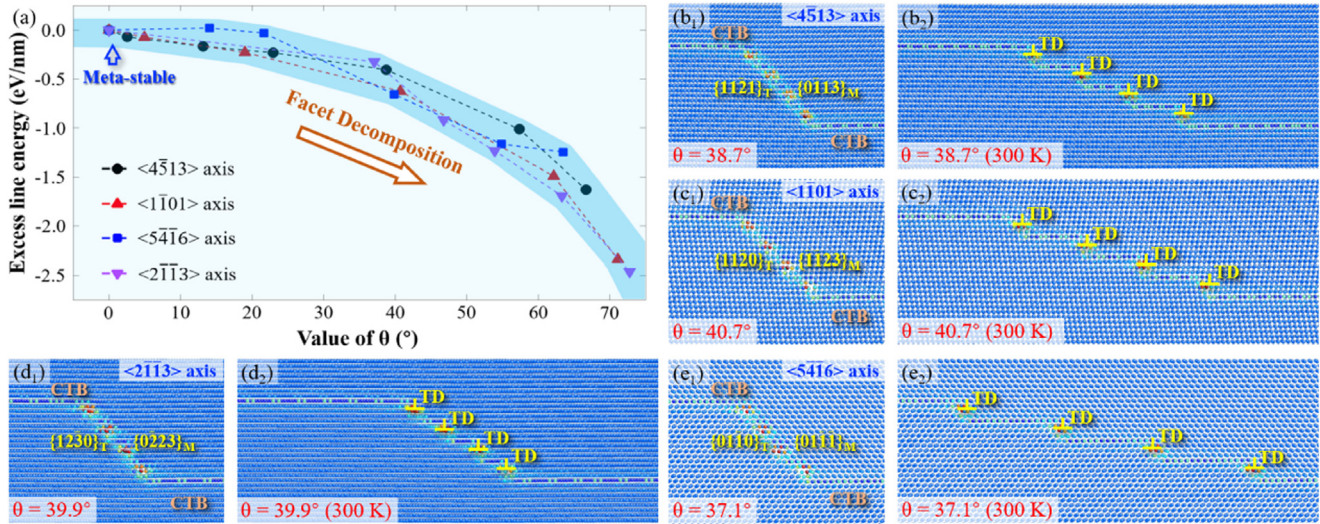
Fig. 4. (a) Excess line energy of structures with respect to value of θ for coherent facets lying parallel to $<4\bar{5}13>$, $<1\bar{1}01>$, $<5\bar{4}\bar{1}6>$ or $<2\bar{1}\bar{1}3>$ axes, respectively. The structure with $\theta = 0.0°$ is set as the reference. (b$_1$) The $\{11\bar{2}1\}_T\|\{0\bar{1}13\}_M$ facet lying parallel to $<4\bar{5}13>$ axis decomposes to (b$_2$) discrete TDs after relaxation at 300 K. (c$_1$) The $\{11\bar{2}0\}_T\|\{\bar{1}\bar{1}23\}_M$ facet lying parallel to $<1\bar{1}01>$ axis decomposes to (c$_2$) discrete TDs after relaxation at 300 K. (d$_1$) The $\{12\bar{3}0\}_T\|\{0\bar{2}23\}_M$ facet lying parallel to $<5\bar{4}\bar{1}6>$ axis decomposes to (d$_2$) discrete TDs after relaxation at 300 K. (e$_1$) The $\{01\bar{1}0\}_T\|\{01\bar{1}\bar{1}\}_M$ facet lying parallel to $<2\bar{1}\bar{1}3>$ axis decomposes to (e$_2$) discrete TDs after relaxation at 300 K.
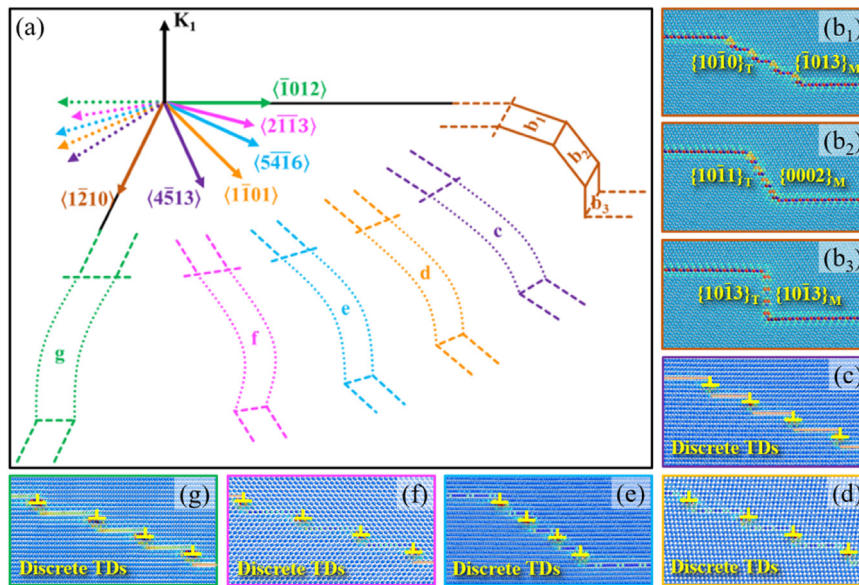
Fig. 5. (a) Schematics showing the twin facets that enclose a non-equilibrium $\{\bar{1}011\}$ twin, including (b$_1$) $\{10\bar{1}0\}_T\|\{\bar{1}013\}_M$, (b$_2$) $\{10\bar{1}1\}_T\|\{0002\}_M$ and (b$_3$) $\{10\bar{1}3\}_T\|\{10\bar{1}3\}_M$ coherent facets lying parallel to $<1\bar{2}10>$ axis, and CTBs with separated TDs in (c) $<4\bar{5}13>$, (d) $<1\bar{1}01>$, (e) $<5\bar{4}\bar{1}6>$ (f) $<2\bar{1}\bar{1}3>$ and (g) $<10\bar{1}2>$ axes.

(Fig. 5(b$_2$)) and $\{10\bar{1}3\}_T\|\{10\bar{1}3\}_M$ (Fig. 5(b$_3$)) coherent facets lying parallel to $<1\bar{2}10>$ axis. In contrast, mixed and screw TDs can hardly pile up, and align separately along CTBs (Fig. 5(c)-(g)).

Different pile-up characteristic between edge TDs and non-edge TDs can be explained by the dissimilar feature of energy profiles associated with edge (Fig. 2(f)), screw (Fig. 3(d)) and mixed (Fig. 4(a)) TDs. With increasing value of θ (more separated TDs), excess line energy associated with edge TDs overall increases with several local minima while that associated with screw/mixed TDs continuously decreases. The local energy minima associated with edge TDs corresponds to formation of three coherent facets in $<1\bar{2}10>$ axis (Fig. 5(b$_1$)-(b$_3$)). The other structures containing edge TDs will transform to one of three coherent facets at 300 K. Meanwhile, screw/mixed TDs cannot smear their cores onto facets, and tend to separate because larger θ results in smaller interaction energy. The difference in feature of energy curves between edge TDs and screw/mixed TDs is contributed by the difference in interface energies. In Fig. 6, we compare the interface energies of coherent facets lying parallel to $<1\bar{2}10>$ and $<10\bar{1}2>$ axes. The interface energies of
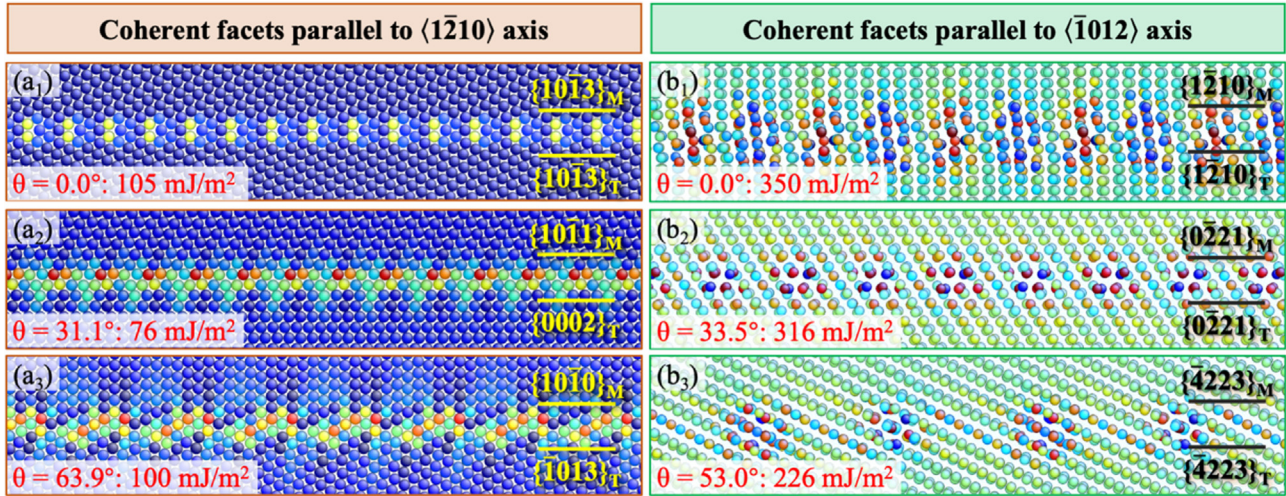
Fig. 6. Atomic structures and interface energies of (a_1) $\{10\bar{1}3\}_T\|\{10\bar{1}3\}_M$, ($a_2$) $\{10\bar{1}1\}_T\|\{0002\}_M$ and (a_3) $\{10\bar{1}0\}_T\|\{\bar{1}013\}_M$ coherent interfaces parallel to <$1\bar{2}10$> axis, and (b_1) $\{1\bar{2}10\}_T\|\{1\bar{2}10\}_M$, ($b_2$) $\{0\bar{2}21\}_T\|\{0\bar{2}21\}_M$ and (b_3) $\{\bar{4}223\}_T\|\{\bar{4}223\}_M$ coherent interfaces parallel to <$10\bar{1}2$> axis.

$\{10\bar{1}3\}_T\|\{10\bar{1}3\}_M$ (Fig. 6(a_1)), $\{10\bar{1}1\}_T\|\{0002\}_M$ (Fig. 6(a_2)) and $\{10\bar{1}3\}_T\|\{10\bar{1}3\}_M$ (Fig. 6(a_3)) coherent facets, corresponding to $\theta = 0.0°$, 31.1° and 63.9°, are relatively low, which are 105 mJ/m^2, 76 mJ/m^2 and 100 mJ/m^2, respectively. The small interface energies thus create the local minima along the energy profile in Fig. 2(f). In contrast, the $\{1\bar{2}10\}_T\|\{1\bar{2}10\}_M$ (Fig. 6(b_1)), $\{0\bar{2}21\}_T\|\{0\bar{2}21\}_M$ (Fig. 6(b_2)) and $\{\bar{4}223\}_T\|\{\bar{4}223\}_M$ (Fig. 6(b_3)) coherent interfaces parallel to <$10\bar{1}2$> axis have relatively high interface energies, which are 350 mJ/m^2, 316 mJ/m^2, 226 mJ/m^2. The interface energies decrease with increasing value of θ. This is because the interfaces are more like TD walls than sharp interfaces since the screw TDs do not smear along the interfaces. Obvious core structures of screw TDs can be observed. Coherent facets with larger θ contain less TDs in unit length, thus owning less core energies and weaker TD interactions. This explains the continuous drop along line energy with increasing θ (Fig. 3(d)). As for twin facets consisting of mixed TD, as shown in Fig. 4(b_1)-(e_1), obvious cores of TDs can be observed, showing similar manner to twin facets with screw TDs. Therefore, the associated energy profiles are similar to that of screw TDs. Discrete mixed TDs are energetically favorable.

4. Twin facets enclosing equilibrium twins

4.1. Semi-coherent facets from coherent facets

To lower the elastic energy associated with TBs that enclose non-equilibrium, misfit dislocations form by dislocation rearrangement and/or emission of lattice dislocations [34,35,47,48]. As shown in Fig. 7, misfit dislocation $\mathbf{b_1}$ with 0.221[10$\bar{1}$2] Burgers vector can form by reaction of two $\langle\mathbf{a}\rangle$ dislocations in twin and matrix that:

$$\mathbf{b_1} = 0.221\left[10\bar{1}2\right]_{M/T} = \frac{1}{3}\left[2\bar{1}\bar{1}0\right]_M + \frac{1}{3}\left[11\bar{2}0\right]_T \quad (1)$$
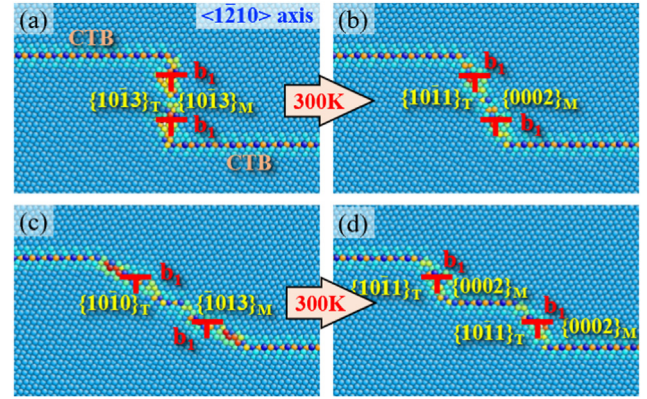

Fig. 7. (a) The $\{10\bar{1}3\}_T\|\{10\bar{1}3\}_M$ semi-coherent facet transforms to (b) the $\{10\bar{1}1\}_T\|\{0002\}_M$ semi-coherent facet after relaxation at 300 K. (c) The $\{10\bar{1}0\}_T\|\{\bar{1}013\}_M$ semi-coherent facet transforms to (d) two $\{10\bar{1}1\}_T\|\{0002\}_M$ semi-coherent facets connected by a CTB.

It is noted that Burgers vector of -$\mathbf{b_1}$ is also nearly equal to Burgers vector of two TDs that:

$$-\mathbf{b_1} = 0.221\left[\bar{1}01\bar{2}\right]_{M/T} \approx 2 \times 0.113\left[\bar{1}01\bar{2}\right]_{M/T} \quad (2)$$

So, formation of two $\mathbf{b_1}$ misfit dislocations on a coherent facet containing four TDs may transform the facet to its fully relaxed state.

The stability of $\{10\bar{1}3\}_T\|\{10\bar{1}3\}_M$, $\{10\bar{1}1\}_T\|\{0002\}_M$ and $\{10\bar{1}0\}_T\|\{\bar{1}013\}_M$ semi-coherent facets, the non-equilibrium states of which are stable, is examined. It is found that only the $\{10\bar{1}1\}_T\|\{0002\}_M$ semi-coherent facet is stable, maintaining its structure after relaxation at 300 K for 500 ps. The $\{10\bar{1}3\}_T\|\{10\bar{1}3\}_M$ semi-coherent facet (Fig. 7(a)) transforms to $\{10\bar{1}1\}_T\|\{0002\}_M$ semi-coherent facet (Fig. 7(b)) through rearrangement of TDs and misfit dislocations. It should be noted that glide of misfit dislocations $\mathbf{b_1}$ (i.e. by synchroshear [34]) is possible since their Burgers vector is parallel to twin plane. The $\{10\bar{1}0\}_T\|\{\bar{1}013\}_M$ semi-coherent facet (Fig. 7(c)) transforms to two shorter $\{10\bar{1}1\}_T\|\{0002\}_M$ semi-coherent
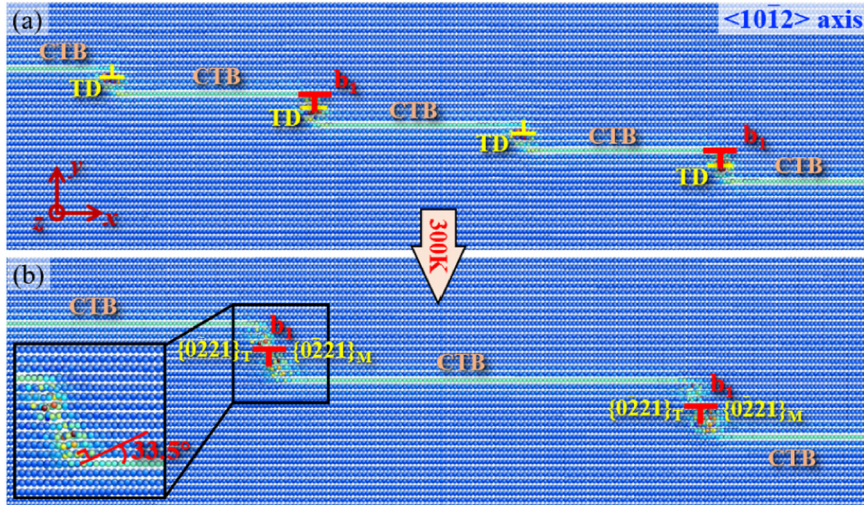
Fig. 8. (a) Discrete screw TDs with line sense parallel to $<10\bar{1}2>$ axis are attracted by misfit dislocations b_1, and transform to (b) $\{0\bar{2}21\}_T\|\{0\bar{2}21\}_M$ semi-coherent facets.

facet connected by CTB (Fig. 7(d)), differing from the long facets as shown in Fig. 7(d). This is because the mobility of TDs is much higher than that of misfit dislocations. The TDs migrate towards misfit dislocations to achieve the low-energy configuration. It should be noted that the simulation results only indicate higher possibility to form $\{10\bar{1}1\}_T\|\{0002\}_M$ semi-coherent facets during twin growth. Thermodynamically, the other types of semi-coherent facets can also form. For example, TDs at twin tips are more likely to pile up vertically under large repelling forces produced by great number of trailing TDs. So, $\{10\bar{1}3\}_T\|\{10\bar{1}3\}_M$ semi-coherent facet could be observed at twin tips.

4.2. Semi-coherent facets from discrete TDs

As for axis non-parallel to $<1\bar{2}10>$, screw/mixed TDs prefers to distribute separately along CTBs. After stress relaxation, an array of discrete TDs should be attracted by misfit dislocation b_1 since they have Burgers vectors with opposite directions. The attraction of TDs aroused by formation of misfit dislocation b_1 results in development of semi-coherent facets. Fig. 8 describes the formation process of a semi-coherent facet lying parallel to $<1\bar{2}10>$ axis. It is found that discrete screw TDs (Fig. 8(a)) migrate towards two misfit dislocations b_1, and pile up onto $\{0\bar{2}21\}_T\|\{0\bar{2}21\}_M$ facets with their plane normal direction 33.5° deviating from twin plane (Fig. 8(b)).

To address the reason that $\{0\bar{2}21\}_T\|\{0\bar{2}21\}_M$ semi-coherent facets form, interface energies of facets lying parallel to $<10\bar{1}2>$ axis are analyzed. Fig. 9 shows the atomic structures of $\{1\bar{2}10\}_T\|\{1\bar{2}10\}_M$, $\{3\bar{8}51\}_T\|\{3\bar{8}51\}_M$, $\{0\bar{2}21\}_T\|\{0\bar{2}21\}_M$ and $\{\bar{4}223\}_T\|\{\bar{4}223\}_M$ semi-coherent interfaces. It is found that the interface energy monotonically decreases with increasing value of θ, mainly resulted from the lowered density of misfit dislocations along interface. Surprisingly, the $\{0\bar{2}21\}_T\|\{0\bar{2}21\}_M$ semi-coherent facet does not have the lowest interface energy. The results suggest

that total energy instead of interface energy should be taken account of.

As shown in Fig. 10, the configuration containing TBs with dimensions L and H in x- and y-directions has their length varying with the value of θ. Total length of CTBs is:

$$l_{CTB} = L - \tan\theta \cdot H \qquad (3)$$

Total length of facet is:

$$l_{facet} = \frac{H}{\cos\theta} \qquad (4)$$

Therefore, for TBs with unit length in z-direction, total interface energy can be summed as:

$$E_{int} = \gamma_{CTB}L + \left(\frac{\gamma_{facet}(\theta)}{\cos\theta} - \gamma_{CTB}\tan\theta\right)H \qquad (5)$$

where γ_{CTB} is interface energy of CTB (77 mJ/m^2) and γ_{facet} is the θ-dependent interface energy of semi-coherent facets. The term $\gamma_{facet}(\theta)/\cos\theta - \gamma_{CTB}\tan\theta$ can be regarded as effective interface energy. If the system tends to achieve the lowest energy state, the effective interface energy should take the smallest value. Fig. 11(f) plots the effective interface energy with respect to θ when zone axis is $<10\bar{1}2>$. When θ is 33.5° (corresponding to $\{0\bar{2}21\}_T\|\{0\bar{2}21\}_M$ facets), the lowest total interface energy can be achieved, which is consistent with the MD simulations (Fig. 8). The effective interface energy associated with semi-coherent facets lying parallel to axes other than $<1\bar{2}10>$ and $<10\bar{1}2>$ axes is plotted in Fig. 11(b)-(e). The effective interface energies associated with $\{14\bar{5}7\}_T\|\{3\bar{4}19\}_M$ ($\theta = 13.2°$), $\{\bar{1}6\bar{5}7\}_T\|\{5\bar{6}17\}_M$ ($\theta = 0°$), $\{\bar{1}4\bar{3}3\}_T\|\{3\bar{4}13\}_M$ ($\theta = 0°$) and $\{01\bar{1}0\}_T\|\{01\bar{1}1\}_M$ ($\theta = 37.1°$) semi-coherent facets lying parallel to $<4\bar{5}13>$, $<1\bar{1}01>$, $<5\bar{4}\bar{1}6>$ and $<2\bar{1}\bar{1}3>$ axes, respectively, are the lowest. Therefore, discrete mixed TDs with various line senses will reassemble around misfit dislocations, and form those semi-coherent facets after stress relaxation. Moreover, as shown in Fig. 11(a), $\{10\bar{1}1\}_T\|\{0002\}_M$ ($\theta = 31.1°$) semi-coherent facet is thermodynamically favorable. This explains
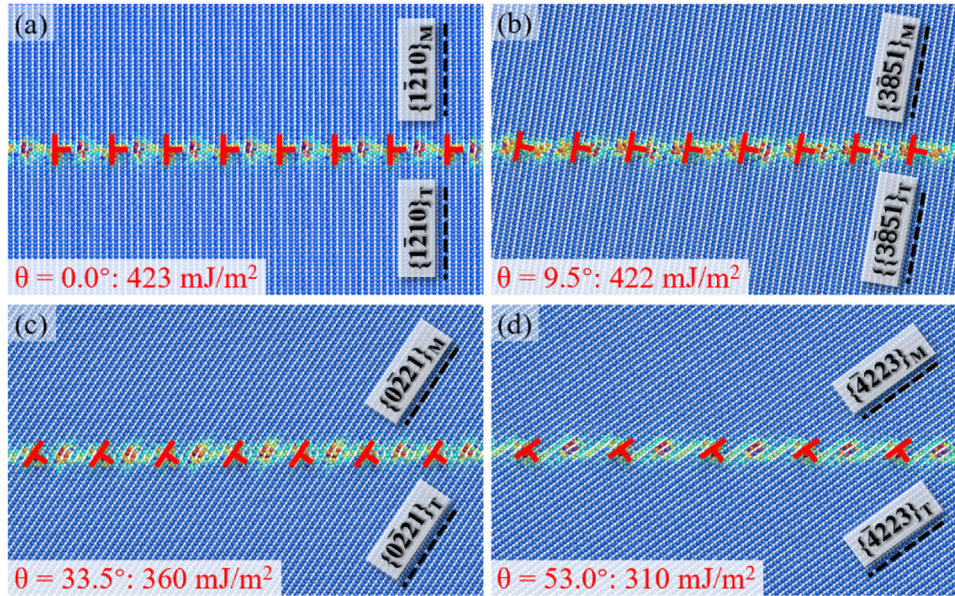
Fig. 9. Atomic structures and interface energies of (a) $\{1\bar{2}10\}_T\|\{1\bar{2}10\}_M$, (b) $\{3\bar{8}51\}_T\|\{3\bar{8}51\}_M$, (c) $\{0\bar{2}21\}_T\|\{0\bar{2}21\}_M$ and (d) $\{\bar{4}223\}_T\|\{\bar{4}223\}_M$ semi-coherent interfaces parallel to $<10\bar{1}2>$ axis.
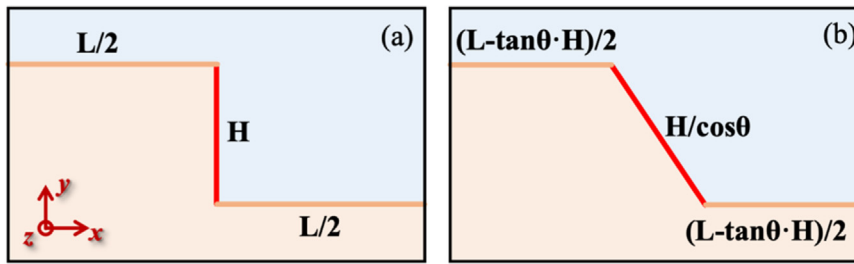

Fig. 10. Schematics illustrating total length of CTBs and facet associated with the configuration containing TBs with dimensions L and H in x- and y-directions.

the formation of $\{10\bar{1}1\}_T\|\{0002\}_M$ semi-coherent facet with various length as shown in Fig. 7.

4.3. Remarks on twin facets enclosing equilibrium twins

Based on the analysis presented above, possible twin facets that enclose 3D equilibrium $\{\bar{1}011\}$ twins are schematically summarized in Fig. 12(a). In general, formation of semi-coherent facets via rearrangement of TDs and misfit dislocations is a thermodynamic process. Therefore, $\{10\bar{1}1\}_T\|\{0002\}_M$ (Fig. 12(b)), $\{14\bar{5}7\}_T\|\{3\bar{4}19\}_M$ (Fig. 12(c)), $\{1\bar{6}57\}_T\|\{5\bar{6}17\}_M$ (Fig. 12(d)), $\{\bar{1}4\bar{3}3\}_T\|\{3\bar{4}13\}_M$ (Fig. 12(e)), $\{01\bar{1}0\}_T\|\{01\bar{1}1\}_M$ (Fig. 12(f)) and $\{0\bar{2}21\}_T\|\{0\bar{2}21\}_M$ (Fig. 12(g)) semi-coherent facets lying parallel to $<1\bar{2}10>$, $<\bar{4}513>$, $<1\bar{1}01>$, $<5\bar{4}\bar{1}6>$, $<2\bar{1}\bar{1}3>$ and $<10\bar{1}2>$ axes, respectively, with the lowest effective interface energy $\gamma_{facet}(\theta)/\cos\theta - \gamma_{CTB}\tan\theta$ are more likely to form. These facets do not necessarily have the lowest crystallographic index, which normally comprises low interface energy. Both interface energy and interaction energy of defects along facets have synergetic effect on low effective interface energy. Moreover, it should be noted that, other than semi-coherent facets concluded in Fig. 12, vertical semi-coherent

facets are very likely to be observed at twin tips. The vertical semi-coherent facets could be transformed from energetically unfavorable vertical TD walls formed under repelling of massive TDs. The predictions can be validated by HRTEM characterization of TBs in different directions.

Three views, along $<1\bar{2}10>$ (Fig. 13(a)), $<1\bar{1}01>$ (Fig. 13(b)) and $<10\bar{1}2>$ (Fig. 13(c)) directions, are adopted for microscopy characterization. The other viewing directions, such as $<4\bar{5}13>$, $<5\bar{4}\bar{1}6>$, $<2\bar{1}\bar{1}3>$, were examined, but cannot produce atomic-scale resolution. It should be noted that twins characterized should be in equilibrium state because the stored stress can easily be relaxed in ultrathin HRTEM sample. Fig. 13(a_1) shows a $\{\bar{1}011\}$ twin viewed in $<1\bar{2}10>$ axis, enclosed by three types of TBs as CTBs (denoted by yellow lines), $\{10\bar{1}1\}_T\|\{0002\}_M$ facets (denoted by yellow lines) and $\{10\bar{1}3\}_T\|\{10\bar{1}3\}_M$ facets (denoted by green lines). For the region far from twin tip (enclosed by the blue rectangle in Fig. 13(a_1)), $\{10\bar{1}1\}_T\|\{0002\}_M$ facets connected by CTBs, which is consistent with the simulation results as shown in Fig. 7(d). As for the region near twin tip (enclosed by the white rectangle in Fig. 13(a_1)), formation of vertical $\{10\bar{1}3\}_T\|\{10\bar{1}3\}_M$ facet (Fig. 13(a_2)) is confirmed. Formation of facets with the other crystallographic index are
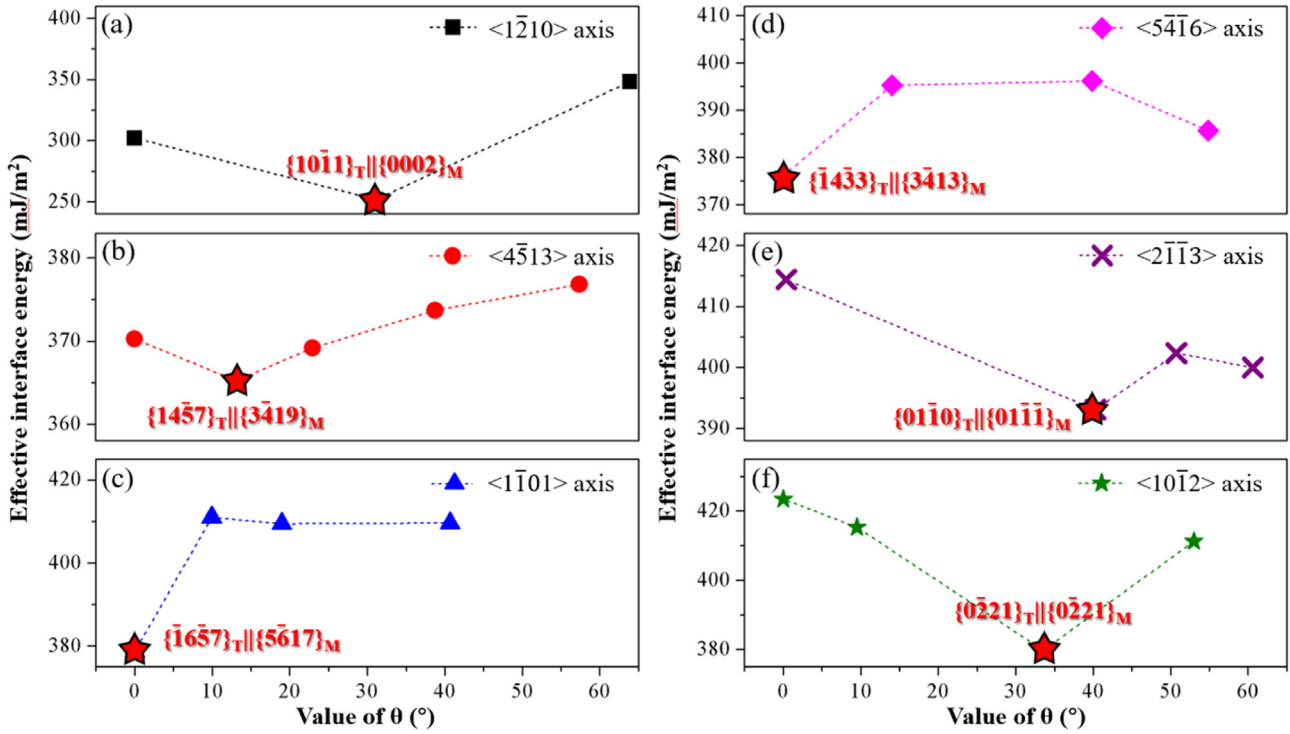
Fig. 11. Effective interface energy with respect to value of θ for semi-coherent facets lying parallel to (a) $<1\bar{2}10>$, (b) $<4\bar{5}13>$, (c) $<1\bar{1}01>$, (d) $<5\bar{4}\bar{1}6>$, (e) $<2\bar{1}\bar{1}3>$ and (f) $<10\bar{1}2>$ axes.
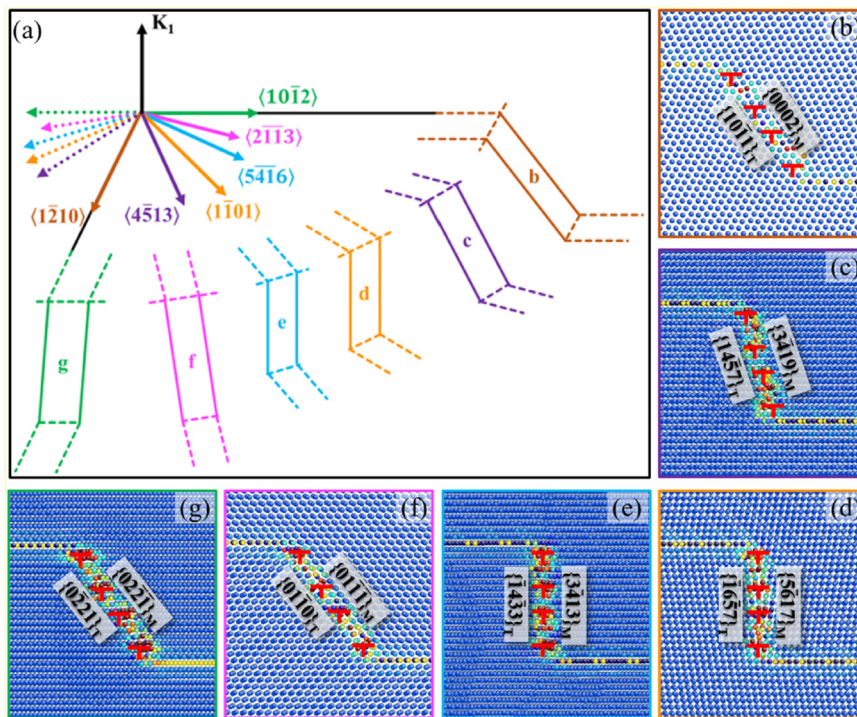

Fig. 12. (a) Schematics showing the TBs that enclose an equilibrium $\{\bar{1}011\}$ twin, including (b) $\{10\bar{1}1\}_T\|\{0002\}_M$ semi-coherent facets in $<1\bar{2}10>$ axis, (c) $\{14\bar{5}7\}_T\|\{3\bar{4}19\}_M$ semi-coherent facets in $<4\bar{5}13>$ axis, (d) $\{\bar{1}6\bar{5}7\}_T\|\{5\bar{6}17\}_M$ semi-coherent facets in $<1\bar{1}01>$ axis, (e) $\{\bar{1}4\bar{3}3\}_T\|\{3\bar{4}13\}_M$ semi-coherent facets in $<5\bar{4}\bar{1}6>$ axis, (f) $\{01\bar{1}0\}_T\|\{01\bar{1}\bar{1}\}_M$ semi-coherent facets in $<2\bar{1}\bar{1}3>$ axis and (g) $\{02\bar{2}1\}_T\|\{0\bar{2}21\}_M$ semi-coherent facets in $<10\bar{1}2>$ axis.
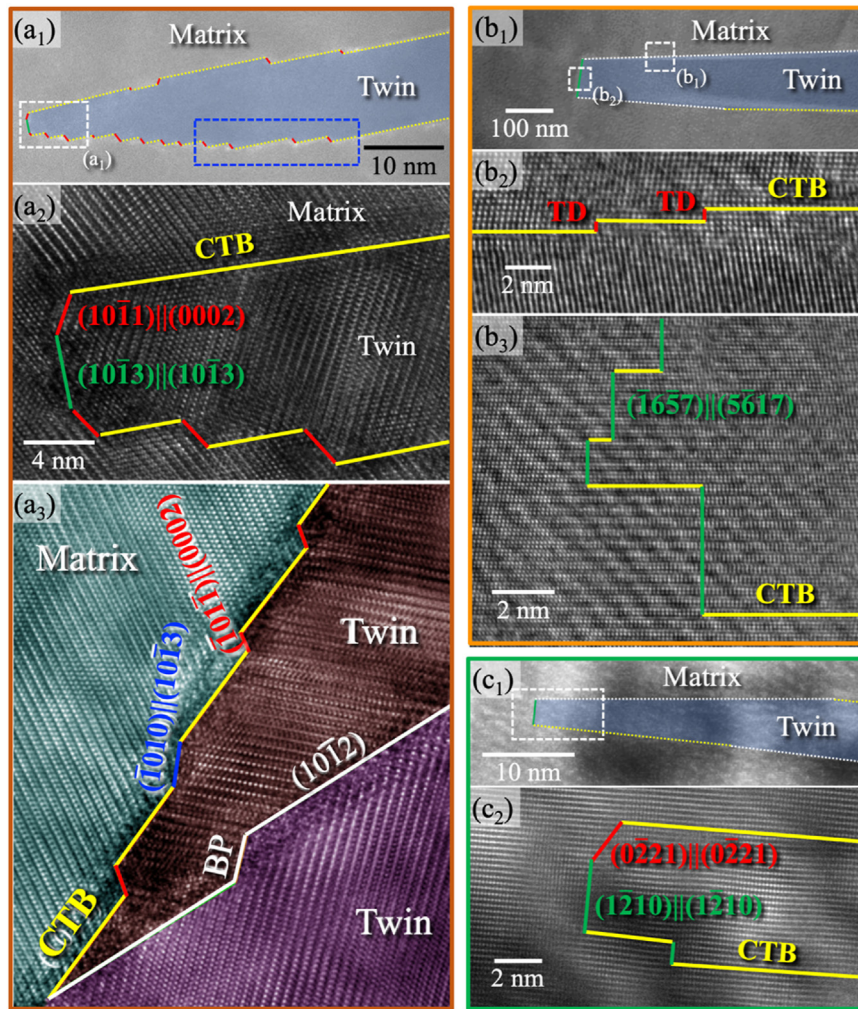
Fig. 13. (a_1) The HAADF image of a $\{\bar{1}011\}$ twin in $<1\bar{2}10>$ view. (a_2) High magnification image of the region enclosed by the white rectangle in (a_1). (a_3) HRTEM showing TBs containing a $\{10\bar{1}0\}_T\|\{\bar{1}013\}_M$ coherent facet as reported in [26]. (b_1) The HAADF image of a $\{\bar{1}011\}$ twin in $<1\bar{1}01>$ view. (b_2) and (b_3) High magnification images of the regions enclosed by the white rectangles in (b_1). (c_1) The HAADF image of a $\{\bar{1}011\}$ twin in $<10\bar{1}2>$ view. (c_2) High magnification images of the region enclosed by the white rectangle in (c_1).

possible, but less likely. Within our knowledge, only Zhang et al. [26] characterized $\{10\bar{1}0\}_T\|\{\bar{1}013\}_M$ facet as shown in Fig. 13(a_3). The morphology of a $\{\bar{1}011\}$ twin in $<1\bar{1}01>$ view is shown in Fig. 13(b_1). TBs far from the twin tip are nearly parallel to twinning plane, indicating the number densities of TDs along those TBs are low. The high magnification image as shown in Fig. 13(b_2) confirms the low number density of TDs. TDs are distanced from each other. In contrast, in the region at twin tip (enclosed by the white rectangle in Fig. 13(b_1)), only $\{\bar{1}6\bar{5}7\}_T\|\{5\bar{6}\bar{1}7\}_M$ facets (green lines in Fig. 13(b_3)) are characterized, which is also concluded in Fig. 12. Fig. 13(c_1) exhibits a $\{\bar{1}011\}$ twin viewed in $<10\bar{1}2>$ axis with its morphology similar to that viewed in $<1\bar{1}01>$ axis. Theoretically, TBs are crystallographically indistinguishable because the projection of twin and matrix is identical [34]. However, local stress field near twin tips enables the identification of TBs. As shown in Fig. 13(c_2), besides the frequently observed vertical $\{1\bar{2}10\}_T\|\{1\bar{2}10\}_M$

facet (green lines), an inclined $\{02\bar{2}1\}_T\|\{02\bar{2}1\}_M$ facet is observed, agreeing with the prediction summarized in Fig. 12.

5. Conclusions

In this study, we propose a general approach that utilizes data of MS/MD simulations to predict twin facets enclosing a 3D twin domain in both non-equilibrium and equilibrium states in HCP metals. We apply this approach to investigate twin boundaries (TBs) associated with 3D $\{\bar{1}011\}$ twins. We also experimentally characterized these facets along $<1\bar{2}10>$, $<1\bar{1}01>$ and $<10\bar{1}2>$ direction to validate the predicted twin facets. Based on these computational and experimental results, we draw the following main conclusions:

- The twin facets that enclose a non-equilibrium twin differ from those that enclose an equilibrium twin in terms of ori-

entation, defect contents, and atomic structures. The stability of the coherent facets associated with a non-equilibrium twin depends on whether the TDs are piled up or discrete. In contrast, the formation of semi-coherent facets associated with an equilibrium twin is accompanied by the formation of misfit dislocations, which leads to a different arrangement of TDs.

- Possible twin facets that enclose a 3D non-equilibrium $\{\bar{1}011\}$ twin include $\{10\bar{1}0\}_T\|\{\bar{1}013\}_M$, $\{10\bar{1}1\}_T\|\{0002\}_M$ and $\{10\bar{1}3\}_T\|\{10\bar{1}3\}_M$ coherent facets lying parallel to $<1\bar{2}10>$ axis via pileup of edge TDs, and discrete non-edge TDs with their line senses parallel to $<4\bar{5}13>$, $<1\bar{1}01>$, $<5\bar{4}16>$ $<2\bar{1}\bar{1}3>$ or $<10\bar{1}2>$ axes aligning separately along CTBs. The easy pileup of the edge TDs results from small interface energy that creates local energy minima preventing repelling between these TDs. It should be noted that the prediction of coherent facets enclosing non-equilibrium twins can hardly be validated by HRTEM since the stored stress associated with non-equilibrium twins can easily be relaxed in ultrathin HRTEM sample.

- Possible twin facets that enclose a 3D equilibrium $\{\bar{1}011\}$ twin include $\{10\bar{1}1\}_T\|\{0002\}_M$, $\{14\bar{5}7\}_T\|\{3\bar{4}19\}_M$, $\{\bar{1}6\bar{5}7\}_T\|\{5\bar{6}17\}_M$, $\{\bar{1}4\bar{3}3\}_T\|\{3\bar{4}13\}_M$, $\{01\bar{1}0\}_T\|\{01\bar{1}1\}_M$ and $\{0\bar{2}21\}_T\|\{0\bar{2}21\}_M$ semi-coherent facets lying parallel to $<1\bar{2}10>$, $<4\bar{5}13>$, $<1\bar{1}01>$, $<5\bar{4}16>$, $<2\bar{1}\bar{1}3>$ and $<10\bar{1}2>$ axes, respectively. These facets have the lowest effective interface energy defined by $\gamma_{\text{facet}}(\theta)/\cos\theta - \gamma_{\text{CTB}}\tan\theta$, but not necessarily have the lowest interface energy γ_{facet}. In addition to the facets with the lowest effective interface energy, vertical semi-coherent facets near the twin tips could be transformed from energetically unfavorable vertical TD walls formed under repelling of between TDs. The prediction of semi-coherent facets lying parallel to $<1\bar{2}10>$, $<1\bar{1}01>$ and $<10\bar{1}2>$ axes that enclose equilibrium twins are validated by HETEM. The other thermodynamically unfavorable facets are less frequently observed. It should be noted that the HRTEM characterization along $<4\bar{5}13>$, $<5\bar{4}16>$ and $<2\bar{1}\bar{1}3>$ axes cannot produce atomic-scale resolution to verify the prediction.

Declaration of Competing Interest

The authors declare that they have no known competing financial interests or personal relationships that could have appeared to influence the work reported in this paper.

Acknowledgments

References

[1] J. Tu, S. Zhang, Mater. Des. 96 (2016) 143–149, doi:10.1016/j.matdes. 2016.02.002.

[2] M. Arul Kumar, I.J. Beyerlein, C.N. Tomé, Acta Mater. 116 (2016) 143–154, doi:10.1016/j.actamat.2016.06.042.

[3] J.W. Christian, S. Mahajan, Prog. Mater Sci. 39 (1) (1995) 1–157, doi:10.1016/0079-6425(94)00007-7.

[4] C. Liu, P. Shanthraj, M. Diehl, F. Roters, S. Dong, J. Dong, W. Ding, D. Raabe, Int. J. Plast. 106 (2018) 203–227, doi:10.1016/j.ijplas.2018. 03.009.

[5] P.G. Partridge, Metall. Rev. 12 (1) (1967) 169–194, doi:10.1179/mtlr. 1967.12.1.169.

[6] L. Wu, A. Jain, D.W. Brown, G.M. Stoica, S.R. Agnew, B. Clausen, D.E. Fielden, P.K. Liaw, Acta Mater. 56 (4) (2008) 688–695, doi:10. 1016/j.actamat.2007.10.030.

[7] M.H. Yoo, Metall. Trans. A 12 (3) (1981) 409–418, doi:10.1007/ BF02648537.

[8] J. Zhang, Q. Yu, Y. Jiang, Q. Li, Int. J. Plast. 27 (5) (2011) 768–787, doi:10.1016/j.ijplas.2010.09.004.

[9] K. Yaddanapudi, M.A. Kumar, J. Wang, X. Wang, T.J. Rupert, E.J. Lavernia, J.M. Schoenung, I.J. Beyerlein, S. Mahajan, J. Mag. Alloy. 11 (1) (2023) 176–191, doi:10.1016/j.jma.2022.11.008.

[10] A. Hadadzadeh, M.A. Wells, J. Mag. Alloy. 1 (2) (2013) 101–114, doi:10.1016/j.jma.2013.04.001.

[11] Q. Zhang, J. Li, K. Jiang, P. Li, Y. Li, Y. Zhang, T. Suo, J. Mag. Alloy. (2021), doi:10.1016/j.jma.2021.10.014.

[12] Z. Wang, X. Zhao, Z. Zhang, Y. Wu, K. Chen, X. Ren, D. Wang, W. Wang, J. Mag. Alloy. (2022), doi:10.1016/j.jma.2022.09.013.

[13] W. Gong, R. Zheng, S. Harjo, T. Kawasaki, K. Aizawa, N. Tsuji, J. Mag. Alloy. 10 (12) (2022) 3418–3432, doi:10.1016/j.jma.2022.02.002.

[14] H.J. Kim, Y.J. Kim, S.H. Park, J. Mag. Alloy. 11 (2) (2023) 671–683, doi:10.1016/j.jma.2021.09.008.

[15] J. Kuang, Y. Zhang, X. Du, J. Zhang, G. Liu, J. Sun, J. Mag. Alloy. (2021), doi:10.1016/j.jma.2021.07.016.

[16] M. Sabbaghian, R. Mahmudi, K.S. Shin, J. Mag. Alloy. 7 (4) (2019) 707–716, doi:10.1016/j.jma.2019.11.001.

[17] Y.M. Zhu, S.W. Xu, J.F. Nie, Acta Mater. 143 (2018) 1–12, doi:10. 1016/j.actamat.2017.09.067.

[18] B.M. Morrow, E.K. Cerreta, R.J. McCabe, C.N. Tomé, Mater. Sci. Eng. A 613 (2014) 365–371, doi:10.1016/j.msea.2014.06.062.

[19] B.M. Morrow, R.J. McCabe, E.K. Cerreta, C.N. Tomé, Metall. Mater. Trans. A 45 (13) (2014) 5891–5897, doi:10.1007/s11661-014-2481-0.

[20] Q. Sun, X.Y. Zhang, R.S. Yin, Y. Ren, L. Tan, Scr. Mater. 108 (2015) 109–112, doi:10.1016/j.scriptamat.2015.06.029.

[21] Q. Sun, X.Y. Zhang, Y. Ren, J. Tu, Q. Liu, Scr. Mater. 90 (91) (2014) 41–44, doi:10.1016/j.scriptamat.2014.07.012.

[22] Q. Sun, X.Y. Zhang, Y.C. Wang, Y. Ren, L. Tan, Q. Liu, Mater. Charact. 116 (2016) 44–47, doi:10.1016/j.matchar.2016.04.005.

[23] J. Tu, X.Y. Zhang, Z.M. Zhou, C. Huang, Mater. Charact. 110 (2015) 39–43, doi:10.1016/j.matchar.2015.10.012.

[24] J. Tu, X.Y. Zhang, Y. Ren, Q. Sun, Q. Liu, Mater. Charact. 106 (2015) 240–244, doi:10.1016/j.matchar.2015.05.032.

[25] J. Wang, L. Liu, C.N. Tomé, S.X. Mao, S.K. Gong, Mater. Res. Lett. 1 (2) (2013) 81–88, doi:10.1080/21663831.2013.779601.

[26] J. Zhang, G. Xi, X. Wan, Mater. Charact. 132 (2017) 280–283, doi:10. 1016/j.matchar.2017.08.021.

[27] J. Zhang, G. Xi, X. Wan, C. Fang, Acta Mater. 133 (2017) 208–216, doi:10.1016/j.actamat.2017.05.034.

[28] Z. Peng, Y. Liu, L. Xiao, Y. Yang, B. Gao, M. Xu, Z. Hu, Y. Yu, X. Chen, H. Zhou, J. Mag. Alloy. (2022), doi:10.1016/j.jma.2022.06. 009.

[29] Z. Zhang, J-H. Peng, J.a. Huang, P. Guo, Z. Liu, S-C. Song, Y. Wang, J. Mag. Alloy. 8 (4) (2020) 1102–1108, doi:10.1016/j.jma.2020.06.012.

[30] J.P. Hirth, J. Wang, C.N. Tomé, Prog. Mater Sci. 83 (2016) 417–471, doi:10.1016/j.pmatsci.2016.07.003.

[31] C.D. Barrett, H. El Kadiri, Acta Mater. 70 (2014) 137–161, doi:10.1016/ j.actamat.2014.02.018.

[32] C.D. Barrett, H. El Kadiri, Scr. Mater. 84 (85) (2014) 15–18, doi:10. 1016/j.scriptamat.2014.03.022.

[33] C.D. Barrett, H. El Kadiri, Acta Mater. 63 (2014) 1–15, doi:10.1016/j. actamat.2013.09.012.

[34] M. Gong, J.P. Hirth, Y. Liu, Y. Shen, J. Wang, Mater. Res. Lett. 5 (7) (2017) 449–464, doi:10.1080/21663831.2017.1336496.

[35] B. Xu, L. Capolungo, D. Rodney, Scr. Mater. 68 (11) (2013) 901–904, doi:10.1016/j.scriptamat.2013.02.023.

[36] A. Ostapovets, P. Molnár, Scr. Mater. 69 (4) (2013) 287–290, doi:10.1016/j.scriptamat.2013.04.019.

[37] A. Ostapovets, A. Serra, Philos. Mag. 94 (25) (2014) 2827–2839, doi:10.1080/14786435.2014.933906.

[38] H. Li, Q. Zeng, P. Yang, Q. Sun, J. Wang, J. Tu, M. Zhu, J. Mater. Sci. Technol. 43 (2020) 230–237, doi:10.1016/j.jmst.2020.01.007.

[39] X.Y. Zhang, B. Li, X.L. Wu, Y.T. Zhu, Q. Ma, Q. Liu, P.T. Wang, M.F. Horstemeyer, Scr. Mater. 67 (10) (2012) 862–865, doi:10.1016/j.scriptamat.2012.08.012.

[40] A. Ostapovets, J. Buršík, R. Gröger, Philos. Mag. 95 (36) (2015) 4106–4117, doi:10.1080/14786435.2015.1115134.

[41] J.P. Hirth, G. Hirth, J. Wang, Proc. Natl Acad. Sci. 117 (1) (2020) 196–204, doi:10.1073/pnas.1915140117.

[42] M. Gong, H. Ma, K. Yang, Y. Liu, J-F. Nie, J. Wang, npj Comput. Mater. 8 (1) (2022) 168, doi:10.1038/s41524-022-00855-y.

[43] S. Xu, P. Zhou, G. Liu, D. Xiao, M. Gong, J. Wang, Acta Mater. 165 (2019) 547–560, doi:10.1016/j.actamat.2018.12.017.

[44] A. Fernández, A. Jérusalem, I. Gutiérrez-Urrutia, M.T. Pérez-Prado, Acta Mater. 61 (20) (2013) 7679–7692, doi:10.1016/j.actamat.2013.09.005.

[45] C. Paramatmuni, Y. Guo, P.J. Withers, F.P.E. Dunne, Int. J. Plast. 143 (2021) 103027, doi:10.1016/j.ijplas.2021.103027.

[46] X. Wan, J. Zhang, X. Mo, F. Pan, J. Mag. Alloy. 7 (3) (2019) 474–486, doi:10.1016/j.jma.2019.05.002.

[47] K. Dang, S. Wang, M. Gong, R.J. McCabe, J. Wang, L. Capolungo, Acta Mater. 185 (2020) 119–128, doi:10.1016/j.actamat.2019.11.070.

[48] M. Gong, G. Liu, J. Wang, L. Capolungo, C.N. Tomé, Acta Mater. 155 (2018) 187–198, doi:10.1016/j.actamat.2018.05.066.

[49] M. Gong, S. Xu, L. Capolungo, C.N. Tomé, J. Wang, Acta Mater. 195 (2020) 597–610, doi:10.1016/j.actamat.2020.05.046.

[50] M. Gong, J. Graham, V. Taupin, L. Capolungo, Acta Mater. 208 (2021) 116603, doi:10.1016/j.actamat.2020.116603.

[51] G. Liu, H. Mo, J. Wang, Y. Shen, Acta Mater. 202 (2021) 399–416, doi:10.1016/j.actamat.2020.11.002.

[52] S. Wang, M. Gong, R.J. McCabe, L. Capolungo, J. Wang, C.N. Tomé, Sci. Adv. 6 (28) (2020) eaaz2600, doi:10.1126/sciadv.aaz2600.

[53] S. Wang, K. Dang, R.J. McCabe, L. Capolungo, C.N. Tomé, Acta Mater. 208 (2021) 116707, doi:10.1016/j.actamat.2021.116707.

[54] J. Wang, S.K. Yadav, J.P. Hirth, C.N. Tomé, I.J. Beyerlein, Mater. Res. Lett. 1 (3) (2013) 126–132, doi:10.1080/21663831.2013.792019.

[55] A. Serra, D.J. Bacon, Philos. Mag. A 54 (6) (1986) 793–804, doi:10.1080/01418618608244438.

[56] A. Luque, M. Ghazisaeidi, W.A. Curtin, Modell. Simul. Mater. Sci. Eng. 21 (4) (2013) 045010, doi:10.1088/0965-0393/21/4/045010.

[57] E. Martínez, L. Capolungo, C.N. Tomé, Phys. Rev. Mater. 2 (8) (2018) 083603, doi:10.1103/PhysRevMaterials.2.083603.

[58] D.E. Spearot, L. Capolungo, C.N. Tomé, Phys. Rev. Mater. 3 (5) (2019) 053606, doi:10.1103/PhysRevMaterials.3.053606.

[59] Y. Liu, P.Z. Tang, M.Y. Gong, R.J. McCabe, J. Wang, C.N. Tomé, Nat. Commun. 10 (1) (2019) 3308, doi:10.1038/s41467-019-10573-7.

[60] J. Wang, I.J. Beyerlein, J.P. Hirth, C.N. Tomé, Acta Mater. 59 (10) (2011) 3990–4001, doi:10.1016/j.actamat.2011.03.024.

[61] J. Wang, J.P. Hirth, C.N. Tomé, Acta Mater. 57 (18) (2009) 5521–5530, doi:10.1016/j.actamat.2009.07.047.

[62] B. Leu, M. Arul Kumar, I.J. Beyerlein, Materialia 17 (2021) 101124, doi:10.1016/j.mtla.2021.101124.

[63] Y. Liu, N. Li, S. Shao, M. Gong, J. Wang, R.J. McCabe, Y. Jiang, C.N. Tomé, Nat. Commun. 7 (1) (2016) 11577, doi:10.1038/ncomms11577.

[64] L. Zou, J. Li, D. Zakharov, E.A. Stach, G. Zhou, Nat. Commun. 8 (1) (2017) 307, doi:10.1038/s41467-017-00371-4.

[65] F. Lednický, J. Hromádková, Z. Pientka, Polymer 42 (9) (2001) 4329–4338, doi:10.1016/S0032-3861(00)00790-4.

[66] A. Serra, D.J. Bacon, R.C. Pond, Acta Metall. 36 (12) (1988) 3183–3203, doi:10.1016/0001-6160(88)90054-5.

[67] P.M. Anderson, J.P. Hirth, J. Lothe, Theory of Dislocations, Cambridge University Press2017.

[68] D.M. Barnett, J. Lothe, J. Phys. F Met. Phys. 4 (10) (1974) 1618, doi:10.1088/0305-4608/4/10/010.

[69] X.Y. Chen, X.F. Kong, A. Misra, D. Legut, B.N. Yao, T.C. Germann, R.F. Zhang, Acta Mater. 143 (2018) 107–120, doi:10.1016/j.actamat.2017.10.012.